

Strong shape dependence of the Morin transition in α -Fe₂O₃ single-crystalline nanostructures

Jun Wang^{1,a}, Victor Aguilar², Le Li¹, Fa-gen
Li¹, Wen-zhong Wang³, and Guo-meng Zhao^{1,2,b}

¹*Department of Physics, Faculty of Science,
Ningbo University, Ningbo, P. R. China*

²*Department of Physics and Astronomy,
California State University, Los Angeles, CA 90032, USA*

³*School of Science, Minzu University of China, Beijing 100081, P. R. China*

Abstract

Single-crystalline hematite (α -Fe₂O₃) nanorings and nanotubes were synthesized by a hydrothermal method. High-resolution transmission electron microscope and selected-area electron diffraction confirm that the axial directions of both nanorings and nanotubes are parallel to the crystalline c -axis. Magnetic measurements show that there exists a first-order Morin transition at about 210 K in the nanoring crystals while this transition disappears in the nanotube crystals. The current results suggest that the Morin transition depends not only on the size, strain, and magnetic field, but also on the shape of nanostructures. This unusual shape dependence of the Morin transition can be explained by a negative surface anisotropy constant in the surface planes parallel to the c -axis and a positive one in the surface planes perpendicular to the c -axis.

Hematite ($\alpha\text{-Fe}_2\text{O}_3$) has a corundum crystal structure and orders antiferromagnetically below its Néel temperature of about 960 K. Bulk hematite exhibits a Morin transition [1] at about 260 K, below which it is in an antiferromagnetic (AF) phase, where the two antiparallel sublattice spins are aligned along the rhombohedral [111] axis. Above the Morin transition temperature T_M , $\alpha\text{-Fe}_2\text{O}_3$ is in the weak ferromagnetic (WF) phase, where the antiparallel spins are slightly canted and lie in the basal (111) plane rather than along [111] axis. The Morin transition is accompanied by the change of the total magnetic anisotropic constant from a negative value at $T > T_M$ to a positive value at $T < T_M$. The rotation of spins by about 90° across this transition is due to the sign change of the magnetic anisotropic constant. Interestingly, this AF-WF transition was found to depend on magnetic field. An applied magnetic field parallel to the rhombohedral [111] axis below T_M was shown [2–4] to induce the spin-flip transition in the entire temperature range below T_M . The AF-WF transition can also be induced by an applied magnetic field perpendicular to the [111] direction [5]. The magnetic structure, the Morin transition, and the field dependence of T_M were explained [5, 6] in terms of phenomenological thermodynamical potential of Dzyaloshinsky.

In recent years, magnetic nanostructures have attracted much attention, not only because of their interesting physical properties but also because of their broad technological applications. Of particular interest is a finite-size effect on ferromagnetic/ferrimagnetic transition temperature. Finite-size effects have been studied in quasi-two-dimensional ultra-thin ferromagnetic films [7–10] and in quasi-zero-dimensional ultra-fine ferromagnetic/ferrimagnetic nanoparticles [11–15]. The studies on thin films [7–10] and more recent studies on nanoparticles [13–15] have consistently confirmed the finite-size scaling relationship predicted earlier [16]. Similarly, a finite-size effect on the Morin transition temperature was observed in nano-sized $\alpha\text{-Fe}_2\text{O}_3$ spherical particles [17–19]. The data show that T_M decreases with decreasing particle size [17, 19], similar to the case of ferromagnetic/ferrimagnetic nanoparticles [13–15]. The reduction in the Morin transition temperature was interpreted as due to inherent lattice strain (lattice expansion) of nano-crystals [17]. For example, an isotropic increase of the lattice spacing by 0.2% in 53 nm nano-crystals leads to a suppression of T_M by about 92 K (Ref. [17]). More recent work [19] showed that the T_M suppression is caused by both strain and the finite-size effect, commonly observed in ferromagnetic/ferrimagnetic materials. Here we show that the Morin transition temperature depends not only on the size, strain and magnetic field, but also on the shape of nanocrystals. The strong shape dependence of

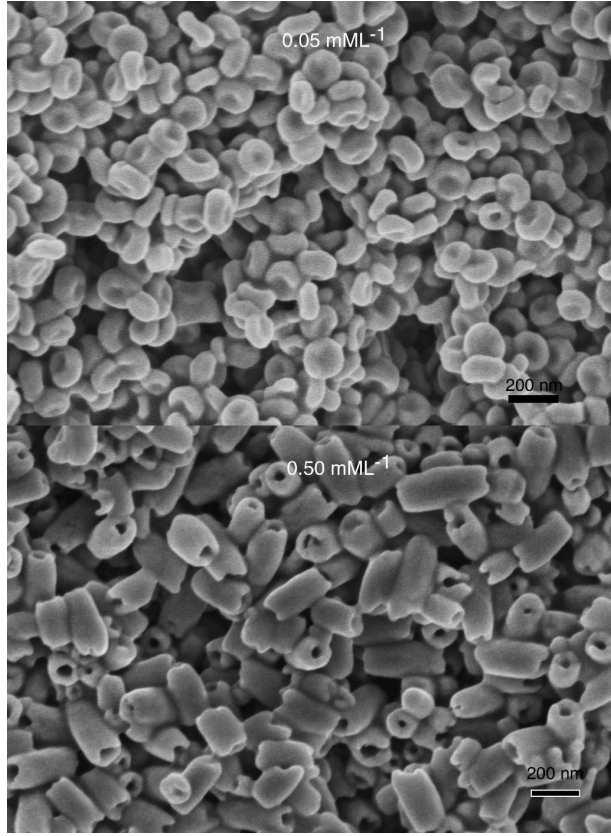


FIG. 1: Scanning electron microscopic images of the two α -Fe₂O₃ nanostructures prepared with different phosphate concentrations. A ring-like morphology is seen in the sample prepared with the phosphate concentration of 0.05 mM/L (upper panel) and a tube-like morphology is observed in the sample prepared with the phosphate concentration of 0.50 mM/L (lower panel). The mean tube length of the nanotubes is about 300 nm.

the Morin transition is quite intriguing considering the fact that the lattice strains of both nanoring and nanotube crystals are similar and small, and that the sizes of nanocrystals are too large (>30 nm) to explain the complete suppression of T_M in the nanotubes. The most likely explanation is that there may exist a negative surface anisotropy constant in the surface planes parallel to the c -axis and a positive one in the surface planes perpendicular to the c -axis.

α -Fe₂O₃ nanorings were prepared by a hydrothermal method, which is similar to that reported in [20]. In the typical process, FeCl₃, NH₄H₂PO₄ (phosphate), and Na₂SO₄ were dissolved in deionized water with concentrations of 0.002, 0.05 and 0.55 mM/L, respectively. After vigorous stirring for 15 min, the mixture was transferred into a Teflon-lined stainless steel autoclave for hydrothermal treatment at 240 °C for 48 h. While keeping all other

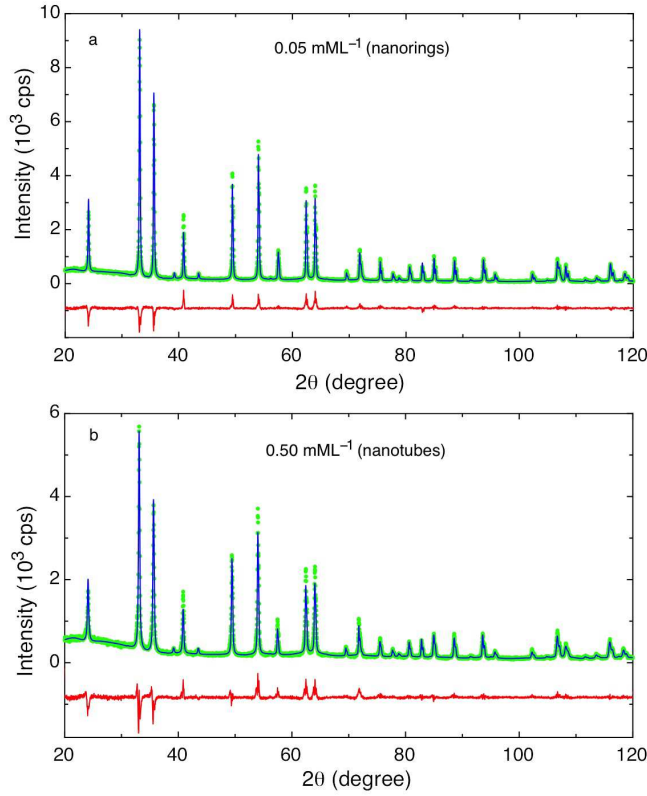


FIG. 2: X-ray diffraction (XRD) spectra of two α - Fe_2O_3 nanostructures prepared with the $\text{NH}_4\text{H}_2\text{PO}_4$ concentrations of 0.05 and 0.50 mM/L, respectively. Rietveld refinement of the XRD data (solid blue lines) with a space group of $R\bar{3}c$ (trigonal hematite lattice) was carried out to obtain the lattice parameters, fractional coordinates of the atoms, and strain information. The red lines represent the differences between the data and the refined curves.

experimental parameters unchanged, increasing the phosphate concentration from 0.05 to 0.50 mM/L to produce α - Fe_2O_3 nanotubes.

The morphology of the samples was analyzed by field emission scanning electron microscopy (FE-SEM, SU70, operated at 3 kV). Figure 1 shows scanning electron microscopic images of the two α - Fe_2O_3 nanostructures prepared with different phosphate concentrations. A ring-like morphology is seen in the sample prepared with the phosphate concentration of 0.05 mM/L (upper panel) and a tube-like morphology is observed in the sample prepared with the phosphate concentration of 0.50 mM/L (lower panel). The mean tube length of the nanotubes is about 300 nm, which is much greater than the mean height (about 60 nm) of the nanorings.

Figure 2 shows x-ray diffraction (XRD) spectra of two α - Fe_2O_3 nanostructures prepared with the $\text{NH}_4\text{H}_2\text{PO}_4$ concentrations of 0.05 and 0.50 mM/L, respectively. The spectra were

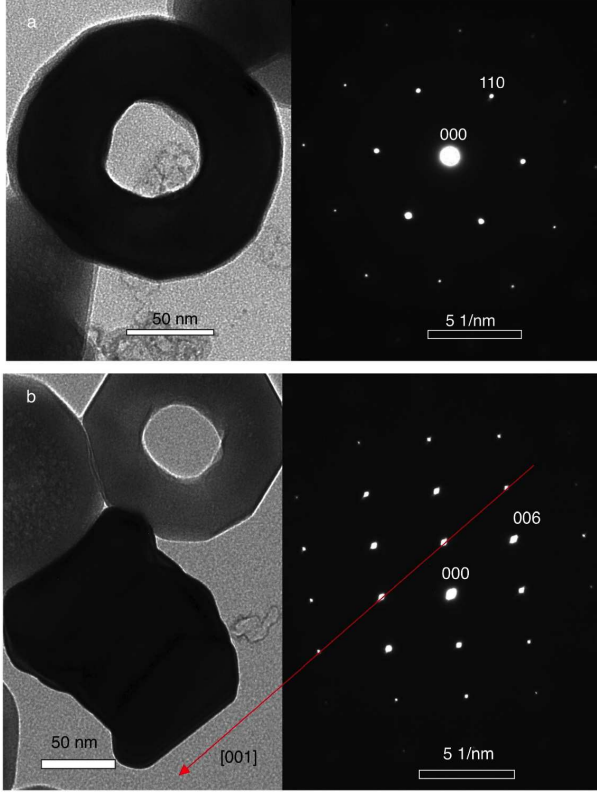


FIG. 3: TEM images (left panels) and SAED patterns (right panels) for a single nanoring.

taken by Rigaku Rint D/Max-2400 X-ray diffractometer. Rietveld refinement of the XRD data (see solid blue lines) with a space group of $R\bar{3}c$ (trigonal hematite lattice) was carried out to obtain the lattice parameters, fractional coordinates of the atoms, and strain information. The lattice parameters obtained from the refinement are as follows: $a = b = 5.0343(6)$ Å, $c = 13.7644(19)$ Å for the nanoring sample, and $a = b = 5.0314(14)$ Å, $c = 13.7771(35)$ Å for the nanotube sample. These parameters are slightly different from those for a bulk hematite [21]: $a = b = 5.0351$ Å, $c = 13.7581$ Å.

In the left panel of Figure 3a, we show transmission electron microscope (TEM) image of a single nanoring (the top view), which was taken by JEOL-2010 with an accelerating voltage of 200 kV. This ring has a wall thickness of about 50 nm, slightly smaller than the average value of 59 nm deduced from the XRD peak widths (see Supplemental Material). The selected-area electron diffraction (SAED) pattern (right panel of Fig. 3a) with a clear hexagonal symmetry indicates that the nanoring is a single crystal with a ring axis parallel to the crystalline c -axis. In order to further prove the single-crystalline nature of the nanoring, we show the side-wall-view of the ring (left panel of Fig. 3b) and the corresponding SAED pattern (right panel of Fig. 3b). The red arrow indicates the $[001]$ direction, which is

determined by the SAED pattern. It is apparent that the ring axis is parallel to the $[001]$ direction or the crystalline c -axis. From the SAED pattern, we can evaluate the c -axis lattice constant. The obtained $c = 13.77(2)$ Å is close to that determined from the XRD data.

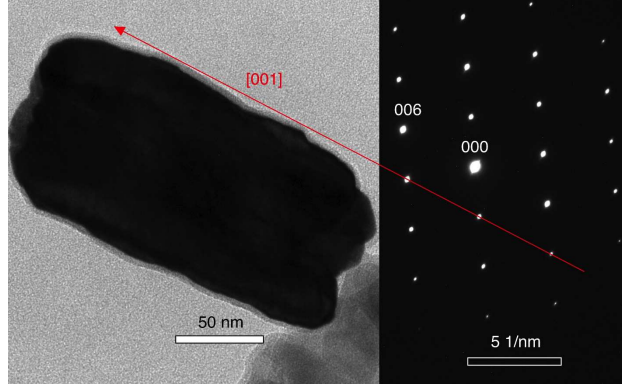


FIG. 4: TEM image (left panel) and SAED pattern (right panel) for a single nanotube.

For the nanotube sample, it is very unlikely to get a top-view TEM image since the axes of the tubes tend to be parallel to the surface of the sample substrate. So we can only take TEM images of individual nanotubes from the side-wall-view. The left panel of Fig. 4 displays a side-wall-view TEM image of a nanotube. The image indicates that the length of the tube is about 200 nm. The single-crystalline nature of the nanotube is clearly confirmed by the SAED pattern (see the right panel of Fig. 4). The red arrow marks the $[001]$ direction, which is determined by the SAED pattern. It is striking that the tube axis is also parallel to the $[001]$ direction.

Figure 5 shows temperature and field dependences of the normalized magnetizations $M(T)/M(350\text{K})$ for the $\alpha\text{-Fe}_2\text{O}_3$ single-crystalline nanorings and nanotubes. Magnetic moment was measured using a Quantum Design vibrating sample magnetometer (VSM) with a resolution better than 1×10^{-6} emu. The samples were initially cooled to 10 K in zero field and a field of 100 Oe was set at 10 K, and then the moment was taken upon warming up to 350 K and cooling down from 350 K to 10 K. At 10 K, other higher fields (1 kOe, 10 kOe, and 50 kOe) were set and the moment was taken upon warming up to 350 K and cooling down from 350 K to 10 K.

It is remarkable that the magnetic behaviors of the two nanostructures are very different. For the nanorings, the low-field magnetization (see Fig. 5a) shows rapid increase around 200 K upon warming, which is associated with the Morin transition. The magnetization below the Morin transition temperature T_M is small (AF state) and it enhances significantly above

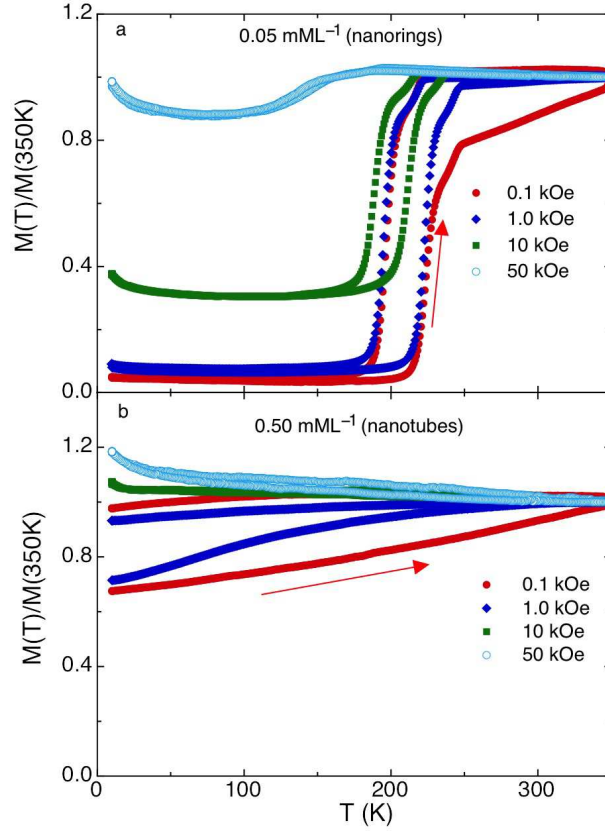


FIG. 5: a) Temperature and field dependencies of the normalized magnetizations $M(T)/M(350K)$ for different $\alpha\text{-Fe}_2\text{O}_3$ single-crystalline nanostructures prepared with two $\text{NH}_4\text{H}_2\text{PO}_4$ concentrations of 0.05 mM/L (nanorings) and 0.50 mM/L (nanotubes), respectively.

T_M (WF state). It is interesting that T_M for warming measurements is significantly higher than that for cooling measurements (the arrows in the figure indicate the directions of the measurements). This difference is far larger than a difference (about 6 K) due to extrinsic thermal lag. This thermal hysteresis was also observed in spherical $\alpha\text{-Fe}_2\text{O}_3$ nanoparticles [19]. The observed intrinsic thermal hysteresis suggests that the nature of the Morin transition is of first-order. The result in Fig. 5a also indicates that the Morin transition temperature decreases with the increase of the applied magnetic field. The zero-field Morin transition temperature in the nanorings is about 210 K (see Supplemental Material). What is striking is that the Morin transition is completely suppressed in the nanotubes (see Fig. 5b). For shorter nanotubes with a mean tube-length of about 100 nm, the Morin transition is broader than that for the nanorings and the zero-field Morin transition temperature is about 188 K (see Supplemental Material).

In Figure 6a, we compare magnetic hysteresis loops at 300 K for the nanorings and

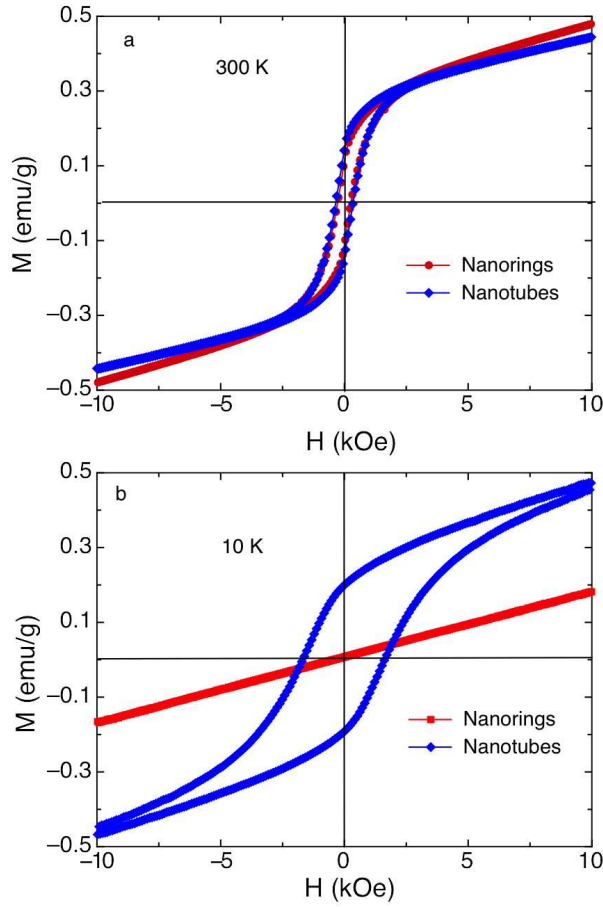


FIG. 6: Magnetic hysteresis loops at 300 K and 10 K for the nanorings and nanotubes. The saturation magnetization M_s , as inferred from a linear fit to the magnetization data above 15 kOe is the same (0.303 ± 0.001 emu/g) for both samples.

nanotubes. There is a subtle difference in the magnetic hysteresis loops of the two samples. The remanent magnetization M_r for the nanotube sample is about 40% higher than that for the nanoring sample, which is related to a higher coercive field in the former sample. However, the saturation magnetization M_s , as inferred from a linear fit to the magnetization data between 15 and 30 kOe, is the same (0.303 ± 0.001 emu/g) for both samples. Fig. 6b shows magnetic hysteresis loops at 10 K for the two samples. It is clear that the nanotube sample remains weak ferromagnetic at 10 K (the absence of the Morin transition down to 10 K) while the nanoring sample is antiferromagnetic with zero saturation magnetization.

The completely different magnetic behaviors observed in the nanoring and nanotube samples are intriguing considering the fact that the two samples have the same saturation magnetization at 300 K and nearly the same lattice parameters. It is known that the lattice strain can suppress T_M according to an empirical relation deduced for spherical nanoparticles

[19]: $\Delta T_M = -600\epsilon$ K, where ϵ is isotropic lattice strain in %. For a uniaxial strain, the formula may be modified as $\Delta T_M = -200\epsilon_i$ K, where ϵ_i is the strain along certain crystalline axis. For the nanoring sample, $a = 5.0343(6)$ Å, which is slightly smaller than (5.0351 Å) for a bulk hematite [21]. This implies that $\epsilon_a = -0.016\%$ for the nanoring sample, in excellent agreement with that (-0.017%) inferred from the XRD peak widths (see Supplemental Material). For the nanotube sample, $a = 5.0314(14)$ Å, so $\epsilon_a = -0.07\%$, in good agreement with that (-0.05%) inferred from the XRD peak widths (see Supplemental Material). The negative strain would imply an increase in T_M according to the argument presented in Ref. [17]. Therefore the suppression of T_M cannot arise from the lattice strains along the a and b directions. On the other hand, the lattice strain along the c direction is positive. Comparing the measured c -axis lattice parameters of the two samples with that for a bulk hematite [21], we can readily calculate that $\epsilon_c = 0.05\%$ for the nanoring sample and 0.14% for the nanotube sample. According to $\Delta T_M = -200\epsilon_i$ K, this leads to the suppression of T_M by 10 K and 28 K for the nanoring and nanotube samples, respectively.

As mentioned above, there is also an independent finite-size effect on T_M unrelated to the strain. For spherical nanoparticles, T_M is suppressed according to $\Delta T_M = -1300/d$ K (Ref. [19]), where d is the mean diameter of spherical particles in nm. For the nanoring and nanotube samples, the smallest dimension is the wall thickness t , which should play a similar role as the diameter of spherical particles [14]. With $t = 58$ nm and 32 nm for the nanoring and nanotube samples, respectively (see Supplemental Material), T_M should be suppressed by 22 K and 41 K, respectively, according to $\Delta T_M = -1300/t$ K. Therefore, due to the strain and finite-size effect, T_M would be reduced from the bulk value of 258 K (Ref. [17]) to 226 K and 189 K for the nanoring and nanotube samples, respectively. For the nanoring sample, the zero-field T_M is about 211 K, which is quite close to the expected value. But for the nanotube sample, the Morin transition is almost completely suppressed, which cannot be explained by the observed strain and the mean wall thickness of the nanotubes.

Another possibility is that the nanotubes may contain more lattice deficiencies than the nanorings. If this were true, the linewidth of the Mössbauer spectrum for the nanotube sample would be broader than that for the nanoring sample because the Mössbauer linewidth is sensitive to disorder, inhomogeneity, and lattice deficiencies. In contrast, the observed linewidth for the nanotube sample is smaller than that for the nanoring sample by 33% (see Supplemental Material). If there would exist substantial lattice deficiencies, they would

mostly be present in surface layers. The narrower Mössbauer linewidth observed in the nanotube sample is consistent with the fact that the nanotubes have a smaller fraction of surface layers.

Finally, we can explain the strong shape dependence of the Morin transition temperature if we assume that the surface magnetic anisotropy constant K_s is negative in the surface planes parallel to the c -axis and positive in the surface planes perpendicular to the c -axis. Indeed a negative value of K_s was found in Ni (111) surface [22] while K_s is positive in Co(0001) surface [23]. For the nanorings, the surface area for the planes parallel to the c -axis are similar to that for the planes perpendicular to the c -axis. Therefore, the total K_s will have a small positive or negative value due to a partial cancellation of the K_s values (with opposite signs) in different surface planes. In contrast, the surface area of a nanotube for the surface planes parallel to the c -axis is much larger than that for the planes perpendicular to the c -axis. This implies that the total K_s in the nanotubes should have a large negative value.

For bulk hematite, the Morin transition temperature is uniquely determined by the total bulk anisotropy constant K at zero temperature [25]. Contributions to K are mainly dipolar anisotropy constant K_{MD} , arising from magnetic dipolar interaction, and fine structure anisotropy (magneto-crystalline anisotropy) K_{FS} , arising from spin-orbit coupling [25]. With $K_{MD} = -9.2 \times 10^6$ erg/cm³ and $K_{FS} = 9.4 \times 10^6$ erg/cm³ in the bulk hematite, the Morin transition temperature was predicted to be $0.281T_N = 270$ K (Ref. [25]), very close to the measured bulk value of 258 K (Ref. [17]).

Following this simple model, we can numerically calculate T_M as a function of $K_{MD}/K_{MD}(\text{bulk})$ on the assumption that K_{FS} remains unchanged, where $K_{MD}(\text{bulk})$ is the bulk anisotropy constant. The calculated result is shown in Fig. 7. It is apparent that T_M is suppressed to zero when the magnitude of K_{MD} increases by 2.2%. Just below this critical point, T_M decreases rapidly with increasing the magnitude of K_{MD} . For nanotubes, contribution of the surface anisotropy is substantial and should be added to the total anisotropy constant. Following the expressions used in Refs. [22, 23], we have $K_{MD} = K_{MD}(\text{bulk}) + 2K_{s\parallel}/t + 2K_{s\perp}/L$, where $K_{s\parallel}$ and $K_{s\perp}$ are the surface anisotropy constants for the planes parallel and perpendicular to the c -axis, respectively, and L is the tube length. Here we have assumed that the surface areas of the inner and outer walls are the same for simplicity. Since T_M for the nanotube sample is just suppressed to zero,

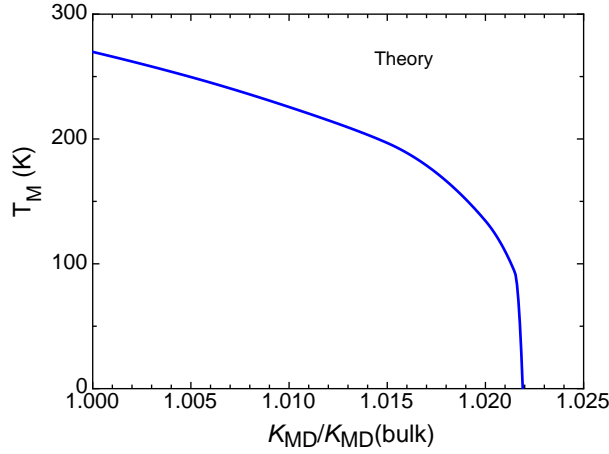


FIG. 7: Numerically calculated T_M as a function of $K_{MD}/K_{MD}(\text{bulk})$, where $K_{MD}(\text{bulk})$ is the bulk anisotropy constant. The calculation is based on a simple model presented in Ref. [25] and on the assumption that K_{FS} remains unchanged.

$K_{MD}/K_{MD}(\text{bulk})$ should be close to 1.022 according to Fig. 7. For shorter nanotubes with $L = 100$ nm and $t = 38$ nm, the zero-field T_M is about 188 K (see Supplemental Material). This implies that T_M in the short nanotubes is suppressed by 70 K. Since the finite-size effect can suppress T_M by 34 K according to $\Delta T_M = -1300/t$ K, the additional suppression of T_M by 36 K should be due to an increase in $|K_{MD}|$ by about 0.79% according to Fig. 7, that is, $K_{MD}/K_{MD}(\text{bulk}) = 1.0079$. With the expression: $K_{MD} = K_{MD}(\text{bulk}) + 2K_{s\parallel}/t + 2K_{s\perp}/L$ and with the L and t values for the two nanotube samples, we yield $K_{s\parallel} = -0.40$ erg/cm² and $K_{s\perp} = 0.68$ erg/cm². The deduced magnitudes of the surface anisotropy constants are in the same order of the experimental values found for Ni and Co [$K_s = -0.22$ erg/cm² for Ni(111) and 0.5 erg/cm² for Co(0001)] [22–24]. Therefore, the observed intriguing experimental results can be naturally explained by a negative surface anisotropy constant in the surface planes parallel to the c -axis and a positive one in the surface planes perpendicular to the c -axis.

In summary, we have prepared single-crystalline hematite nanorings and nanotubes using a hydrothermal method. High-resolution transmission electron microscope and selected-area electron diffraction confirm that the axial directions of both nanorings and nanotubes are parallel to the crystalline c -axis. Magnetic measurements show that there exists a first-order Morin transition at about 210 K in the nanoring crystals while this transition disappears in nanotube crystals. The current results suggest that the Morin transition depends not only on the size, strain and magnetic field, but also on the shape of nanostructures. This unusual

shape dependence of the Morin transition can be explained by a negative surface anisotropy constant in the surface planes parallel to the c -axis and a positive one in the surface planes perpendicular to the c -axis.

Acknowledgment: This work was supported by the National Natural Science Foundation of China (11174165), the Natural Science Foundation of Ningbo (2012A610051), and the K. C. Wong Magna Foundation.

^a wangjun2@nbu.edu.cn

^b gzhao2@calstatela.edu

Supplemental Material

I. Scanning electron microscopic images of nanorings and nanotubes

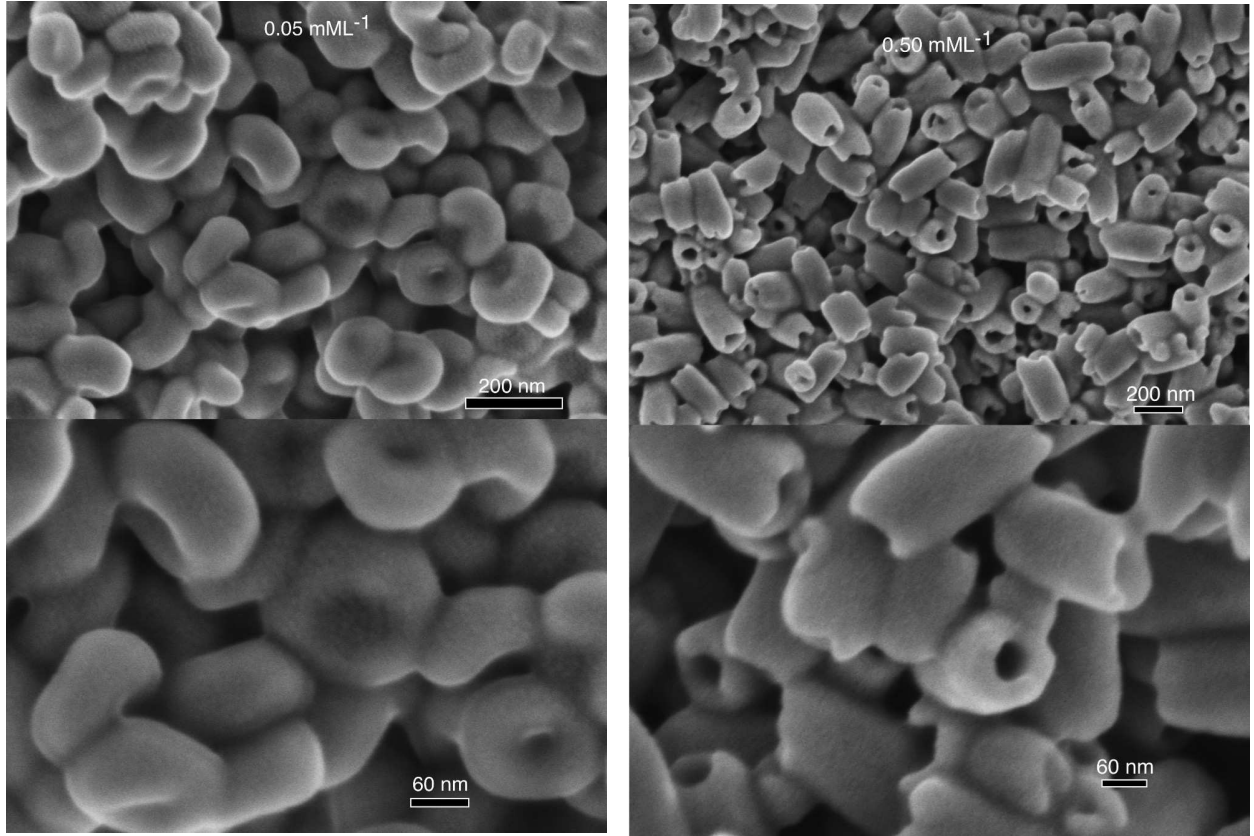


FIG. 8: Scanning electron microscopic images of the α -Fe₂O₃ nanorings (left panels) and nanotubes (right panels).

Figure 8 shows scanning electron microscopic (SEM) images of the two α -Fe₂O₃ nanostructures prepared with the NH₄H₂PO₄ concentrations of 0.05 mM/L (left panels) and 0.50

mM/L (right panels), respectively. For the sample prepared with a low $\text{NH}_4\text{H}_2\text{PO}_4$ concentration, the morphology of the nanostructures is ring-like. The SEM images appear to indicate that most nanorings have no or very small central holes. The mean thickness of the rings along the radial direction is similar to that along the axial direction. From the more magnified SEM image shown in the left-lower panel, the mean thickness of the rings is estimated to be about 60 nm. For the sample prepared with a high $\text{NH}_4\text{H}_2\text{PO}_4$ concentration, the morphology of the nanostructures is tube-like. The mean wall thickness of the tubes and the mean tube length are estimated to be about 30 nm and 300 nm, respectively.

II. Transmission electron microscopic images of nanorings and nanotubes

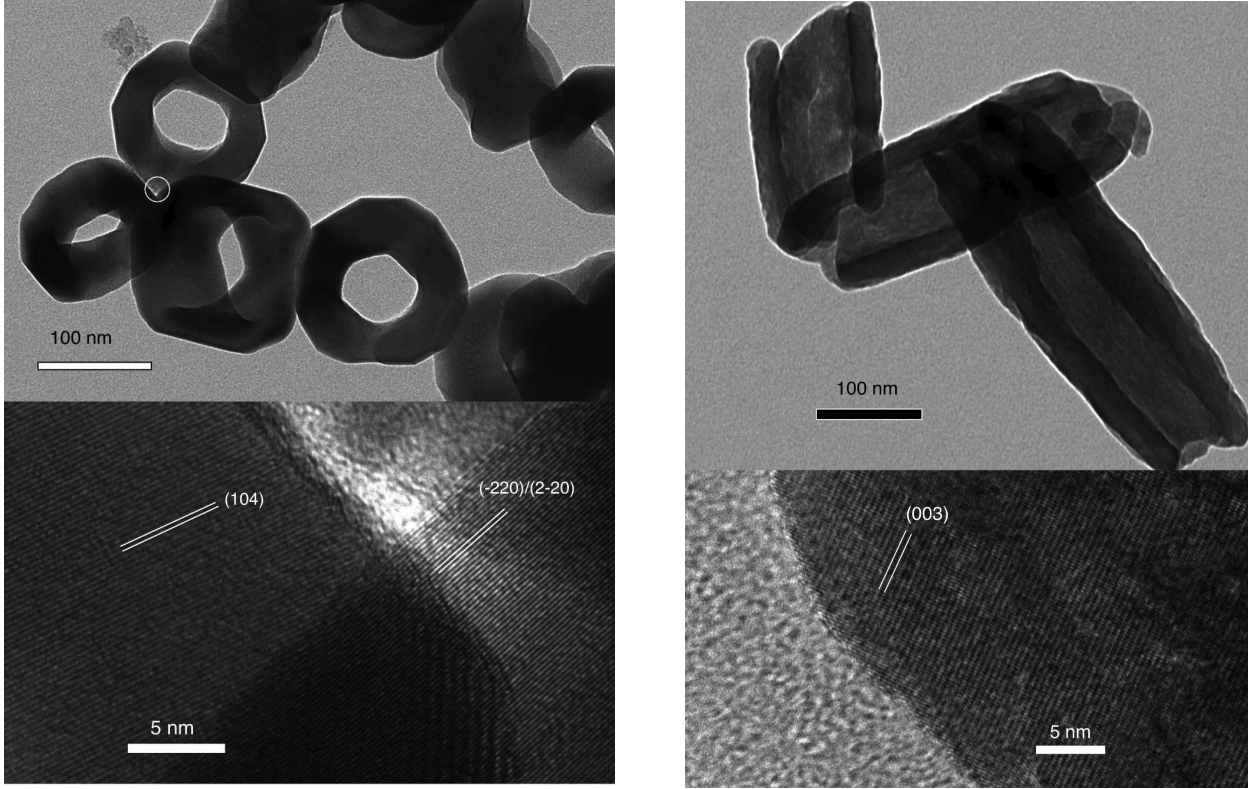


FIG. 9: Transmission electron microscopic (TEM) and high-resolution transmission electron microscopic (HRTEM) images of the nanorings (left panels) and the nanotubes (right panel)

Figure 9 shows transmission electron microscopic (TEM) and high-resolution transmission electron microscopic (HRTEM) images of the nanorings (left panels) and nanotubes (right panels). In contrast to the SEM images, the TEM image shown in the left-upper panel appears to indicate that the most rings have central holes. This image is not representative since it only samples a small number of the rings in a selected area. A TEM image covering

a larger area is shown in Fig. 10 below. It is clear that about 40% of the rings have central holes. In the left-lower panel of Fig. 9, we show a HRTEM image for the selected area marked by a circle in the left-upper panel. The image covers the two surfaces of two different rings; one is the top surface of the ring perpendicular to the ring axis and another is the outer-wall surface of the ring parallel to the ring axis. The exposed surfaces are different in the two rings. For the top surface of the ring, the average distance between the adjacent planes (marked by two parallel lines) is 0.220 nm, suggesting that these are (-220) or $(2-20)$ planes. For the outer-wall surface of the ring, the average distance between the adjacent planes is 0.270 nm, which indicates that these are (104) planes. From the HRTEM images, it is also apparent that the surfaces are smooth and the density of lattice deficiencies is not substantial.

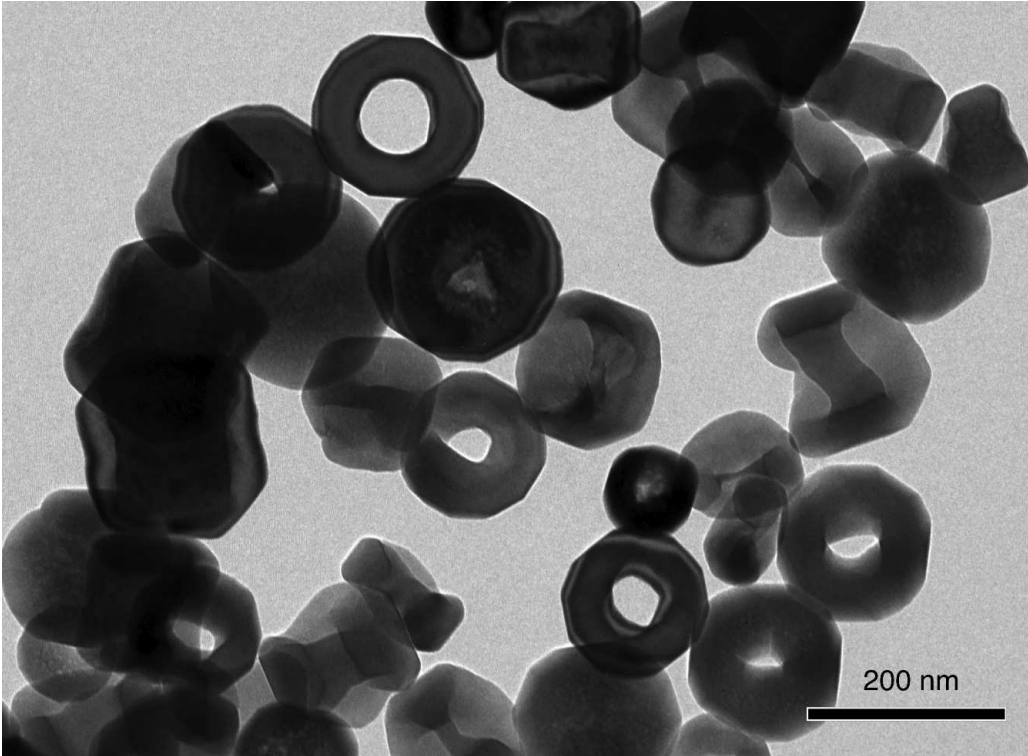


FIG. 10: TEM image of the nanorings in a larger area. About 40% of the rings have central holes.

The TEM image displayed in the right-upper panel of Fig. 9 sees three nanotubes. The wall-thickness of these tubes is in the range of 25-50 nm, in reasonable agreement with the mean wall thickness (about 32 nm) determined from the x-ray diffraction (XRD) peak widths (see section III below). The HRTEM image (right-lower panel) was taken from the outer-wall surface of the tube. The average distance between the adjacent planes is 0.460 nm, implying

that these are (003) planes. This is consistent with the selected area electron diffraction (SAED) pattern shown in Fig. 3b of the main text, which clearly demonstrates that the tube axis is parallel to the crystalline c -axis.

III. Peak widths of the x-ray diffraction spectra: Determination of the mean wall thickness and strain

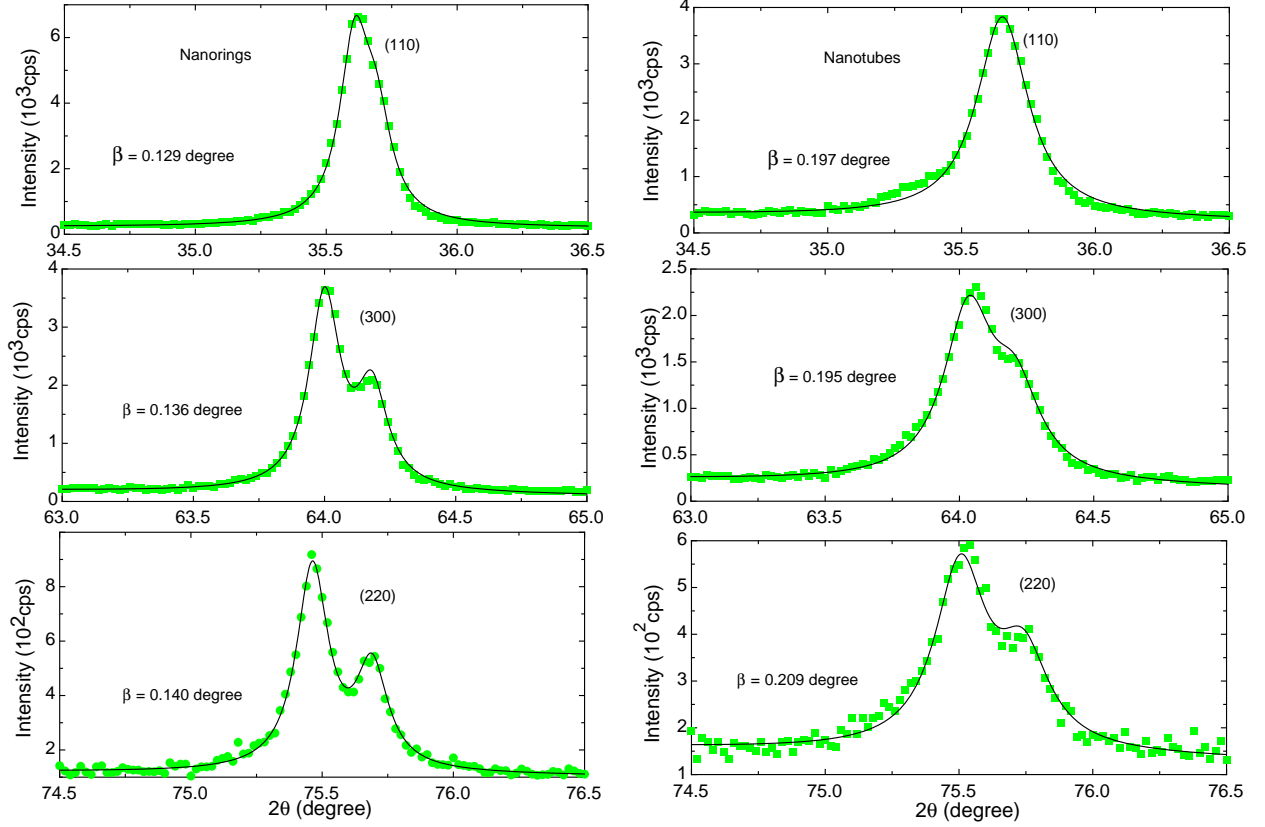


FIG. 11: X-ray diffraction spectra of the (110), (300), and (220) peaks for the nanorings (left panel) and nanotubes (right panel). The peaks are best fitted by two Lorentzians (solid lines), which are contributed from the Cu $K_{\alpha 1}$ and $K_{\alpha 2}$ radiations. The intrinsic peak width β (after correcting for the instrumental broadening) is indicated in each figure.

Since the axes of both nanorings and nanotubes are parallel to the crystalline c -axis (see main text), the mean wall thickness of the nanorings and nanotubes can be quantitatively determined by the peak widths of the x-ray diffraction peaks that are associated with the diffraction from the planes perpendicular to the c -axis. Figure 11 shows x-ray diffraction spectra of the (110), (300), and (220) peaks for the nanoring and nanotube samples. The peaks are best fitted by two Lorentzians (solid lines) contributed from the Cu $K_{\alpha 1}$ and $K_{\alpha 2}$

radiations. The fit has a constraint that the ratio of the $K_{\alpha 1}$ and $K_{\alpha 2}$ intensities is always equal to 2.0.

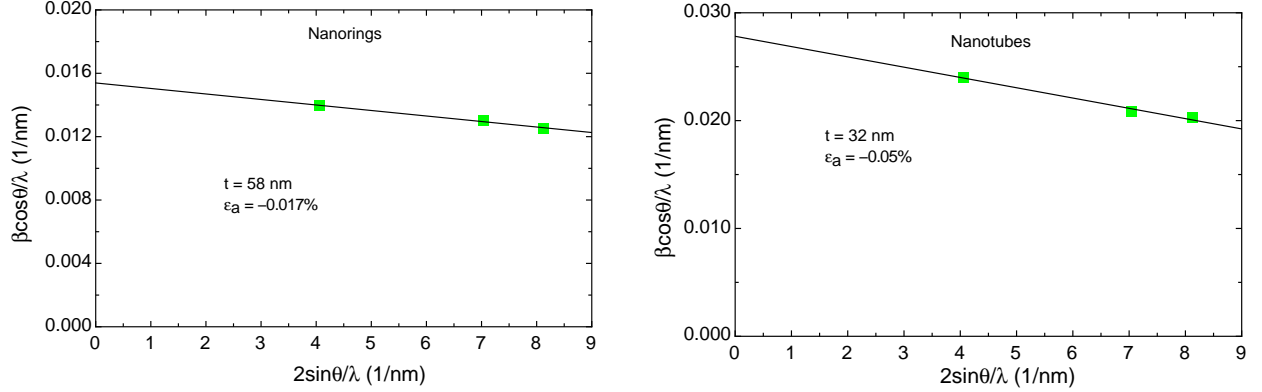


FIG. 12: Dependence of $\beta \cos \theta / \lambda$ on $2 \sin \theta / \lambda$ for the nanotings and nanotubes. The linear lines are the fitted curves of Eq. 1. The fitting parameters are indicated in each figure

It is known that the x-ray diffraction peaks are broadened by strain, lattice deficiencies, and small particle size. When the density of lattice deficiencies is negligibly small, the broadening is contributed from both strain ϵ and particle size t . In this case, there is a simple expression [26]:

$$\frac{\beta \cos \theta}{\lambda} = \frac{0.89}{t} + \frac{2\xi \sin \theta}{\lambda}, \quad (1)$$

where the first term is the same as Scherrer's equation that is related to the particle size t , the second term is due to strain broadening, and ξ was found to be close to 2ϵ (Ref. [27]). In Fig. 12, we plot $\beta \cos \theta / \lambda$ versus $2 \sin \theta / \lambda$ for the nanotings and nanotubes. According to Eq. 1, a linear fit to the data gives information about the mean wall thickness t and strain ϵ_a along a and b axes. The strain is small and negative for both samples (see the numbers indicated in the figures). It is interesting that the magnitudes of the strain inferred from the XRD peak widths are very close to those found directly from the measured lattice parameters. For example, the strain is found to be -0.07% from the lattice parameters for the nanotubes (see main text), in excellent agreement with that (-0.05%) inferred from the XRD peak widths.

IV. Field dependence of the Morin transition temperature in nanorings

The result in Fig. 5a of the main text suggests that the Morin transition temperature decreases with the increase of the applied magnetic field. In Figure 13, we show the plot of

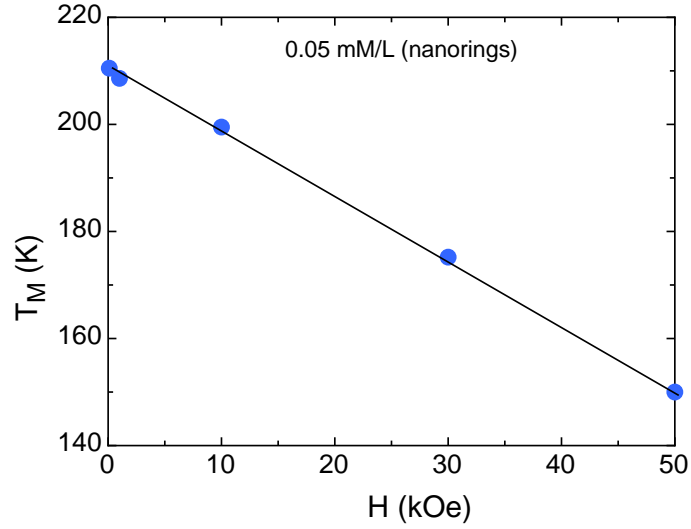


FIG. 13: Magnetic field dependence of the Morin transition temperature T_M in the nanoring sample. The zero-field T_M is 210.5 K.

T_M versus applied magnetic field H for the nanoring sample. Here T_M is a simple average of the warming and cooling T_M 's, which are defined as the midpoint temperatures in the transition range. It is evident that T_M decreases linearly with increasing magnetic field, in agreement with the previous result [19]. The zero-field T_M is 210.5 K, which is close to the expected value from the measured strain and particle-size (see the main text).

V. Room-temperature Mössbauer spectra for the nanorings and nanotubes

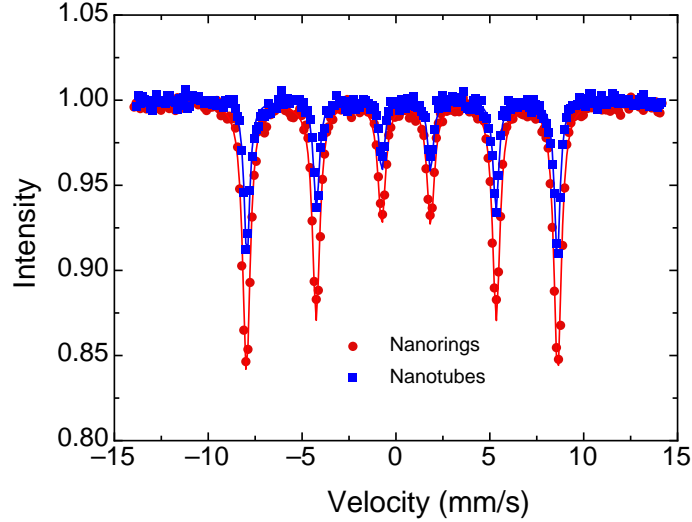


FIG. 14: Room-temperature Mössbauer spectra for the nanorings and nanotubes.

TABLE I: The fitting parameters for the room-temperature Mössbauer spectra of the nanorings and nanotubes

	Half width (mm/s)	Hyperfine field (kOe)	Isomer shifts (mm/s)	Quadrupole shifts (mm/s)
Nanorings	0.24	513.30	0.44	-0.22
Nanotubes	0.18	511.85	0.44	-0.22

It is known that the linewidth of a Mössbauer spectrum is sensitive to disorder, inhomogeneity, and lattice deficiencies. If the nanotubes would contain more lattice deficiencies than the nanorings, the Mössbauer linewidth for the nanotube sample would be broader than that for the nanoring sample. In Fig. 14, we show room-temperature Mössbauer spectra for the nanorings and nanotubes. The spectra are fitted by a single sextet (solid lines) with the fitting parameters displayed in Table I. It is apparent that the linewidth for the nanotube sample is smaller than that for the nanoring sample by 33% while all other parameters are the same within the uncertainties. The much narrower linewidth for the nanotube sample implies less lattice deficiencies, disorder, and/or inhomogeneity. Therefore, it is unlikely that the absence of the Morin transition in the nanotube sample is caused by more lattice deficiencies and/or disorder.

VI. Morin transition in short nanotubes

In the main text, we have shown that there is a first-order Morin transition in the nanorings and this transition is almost completely suppressed in the nanotubes with the mean tube length of about 300 nm and mean wall thickness of 32 nm. Now a question arises as to how the Morin transition depends on the tube length while the wall thickness remains similar. We have prepared short nanotubes using the same starting materials as the nanorings but with a slightly lower hydrothermal treatment temperature (220 °C rather than 240 °C).

Figure 15 displays a SEM image of the short nanotubes. It is clear that the mean tube length of the short nanotubes is about 100 nm and the mean wall thickness is about 40 nm. From Rietveld refinement of the XRD spectrum of this sample, we obtain the lattice parameters: $a = b = 5.0302(10)$ Å, $c = 13.7576(28)$ Å. The a -axis lattice parameter for the short nanotubes is very close to that ($5.0314(14)$ Å) for the long nanotubes and the c -axis

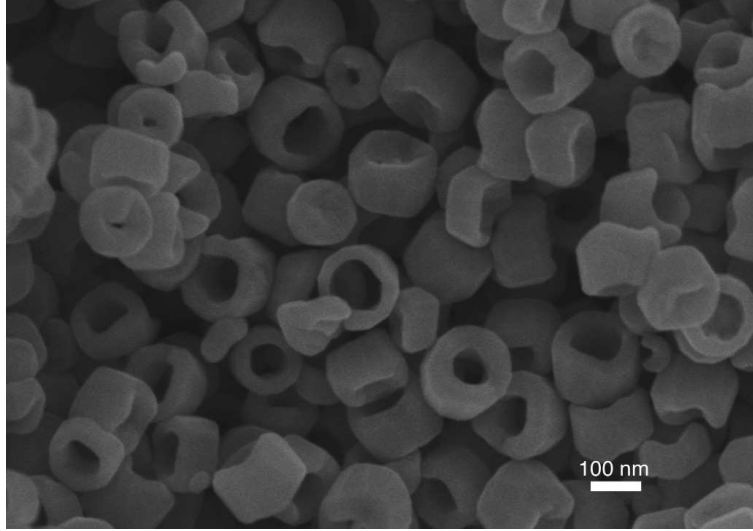


FIG. 15: SEM image of the short nanotubes

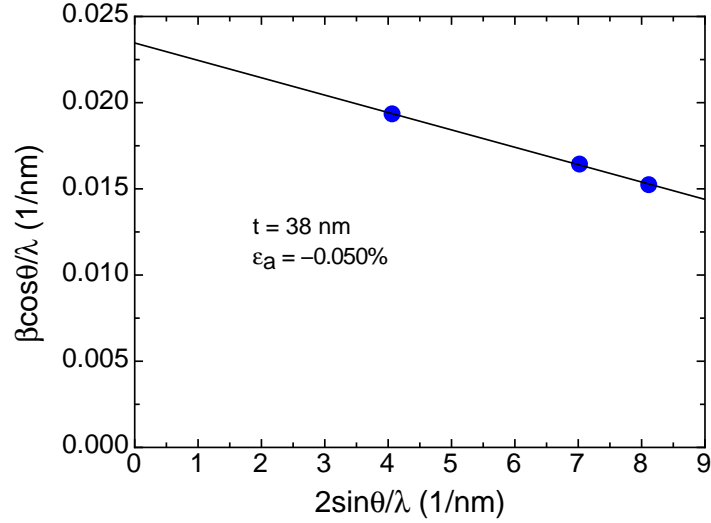


FIG. 16: Dependence of $\beta \cos \theta / \lambda$ on $2 \sin \theta / \lambda$ for the short nanotubes. The linear line is the fitted curve of Eq. 1 and the fitting parameters are indicated in the figure.

parameter is similar to that (13.7644(19) Å) for the nanorings. The mean wall thickness and strain are determined by the XRD peak widths displayed in Fig. 16. The mean wall thickness of the short tube is 38 nm, slightly larger than that (32 nm) for the long nanotubes. The strain for the short nanotubes is the same as that for the long nanotubes. This is consistent with the same a -axis lattice constant found for the short and long nanotubes.

Figure 17 show temperature dependence of the magnetic susceptibility for the short nanotubes, measured in a magnetic field of 1 kOe. The Morin transition is clearly seen in the short nanotubes. There seem to be two transitions with slightly different Morin transition

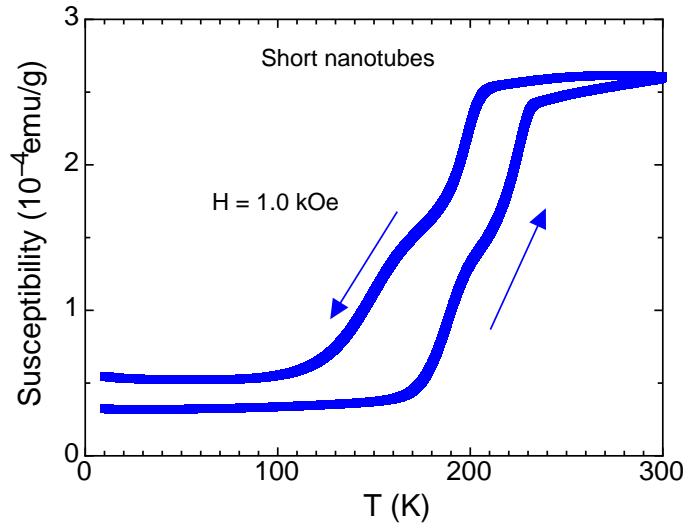


FIG. 17: Temperature dependence of the magnetic susceptibility for the short nanotubes, measured in a magnetic field of 1 kOe. The mean Morin transition temperature for the warming and cooling measurements is 188 K.

temperatures. The reason for this is unclear. If the Morin transition temperature is defined as the mid-point temperatures of the transition, T_M is 201 K for the warming measurement and 174 K for the cooling measurement. The average value is 188 K. Compared with the bulk value of 258 K, the Morin transition temperature in the short nanotubes is suppressed by 70 K. It is interesting that the Morin transition for the short nanotubes is about 22 K lower than that (210 K) for the nanorings. The difference is partly due to the finite-size effect, which can account for 12 K difference in T_M . The remaining 10 K difference should be caused by a longer tube length in the short nanotubes than in the nanorings.

Acknowledgment: This work was supported by the National Natural Science Foundation of China (11174165), the Natural Science Foundation of Ningbo (2012A610051), and the K. C. Wong Magna Foundation.

^a wangjun2@nbu.edu.cn

^b gzhao2@calstatela.edu

[1] Morin, F. J. Phys. Rev. **1950**, 78, 819.

[2] Besser, P. J.; Morrish, A. H. Phys. Lett. **1964**, 13, 289.

- [3] Foner, S.; Williamson, S. J. J. Appl. Phys. **1965**, 36, 1154.
- [4] Hirone, T. J. Appl. Phys. **1965**, 36, 988.
- [5] Flanders, F. J.; S. Shtrikman, Solid State Communi. **1965**, 3, 285.
- [6] Dzyaloshinsky, I. E. Phys. Chem. Solids **1958**, 4, 241.
- [7] Huang, F.; Mankey, G. J.; Kief, M. T.; Willis, R. F. J. Appl. Phys. **1993**, 73, 6760.
- [8] Li, Y.; Baberschke, K. Phys. Rev. Lett. **1992**, 68, 1208.
- [9] Elmers, H. J.; Hauschild, J.; Hoche, H.; Gradmann, U.; Bethge, H.; Heuer, D.; Kohler, U. Phys. Rev. Lett. **1994**, 73, 898.
- [10] Schneider, C. M.; Bressler, P.; Schuster, P.; Kirschner, J. de Miguel, J. J.; Miranda, R. Phys. Rev. Lett. **1990**, 64, 1059.
- [11] Tang, Z. X.; Sorensen, C. M.; Klaboune, K. J. Phys. Rev. Lett. **1991**, 67, 3602.
- [12] Du, Y.W.; Xu, M. X.; Wu, J.; Dhi, Y. B.; Lu, H. X.; Xue, R. H. J. Appl. Phys. **1991**, 70, 5903.
- [13] Wang, J.; Wu, W.; Zhao, F.; Zhao, G. M. Appl. Phys. Lett. **2011**, 98, 083107.
- [14] Wang, J.; Wu, W.; Zhao, F.; Zhao, G. M. Phys. Rev. B **2011**, 84, 174440.
- [15] Wang, J.; Zhao, F.; Wu, W.; Zhao, G. M. J. Appl. Phys. **2011**, 110, 123909.
- [16] Fisher, M. E.; Barber, M. N. Phys Rev Lett **1972**, 28, 1516.
- [17] Schroer, D.; Nininger, Jr., R. C. Phys. Rev. Lett. **1967**, 19, 632.
- [18] Gallagher, P. K.; Gyorgy, E. M. Phys. Rev. **1969**, 180, 622.
- [19] Muench, G. J.; Araj, S.; Matijevic, E. Phys. Stat. Sol. **1985**, 92, 187.
- [20] Jia, C. J. *et al.* J. Am. Chem. Soc. **2008**, 130, 16968.
- [21] Hill, A. H.; Jiao, F.; Bruce, P. G.; Harrison, A.; Kockelmann, I. W.; Ritter, C. Chem. Mater. **2008**, 20, 4891.
- [22] Gradmann, U.; Bergholz, R.; Bergter, E. **1984**, Mag-20, 1840. The sign of the surface anisotropy constant in the original paper is incorrect, as pointed out in Ref. [23]. The correct sign was also quoted in Ref. [24]
- [23] Chappert, C.; Le Dang, K.; Beauvillain, P.; Hurdequint, H.; Renard, D. Phys. Rev. B **1986**, 34, 3192.
- [24] Bruno, P. J. Appl. Phys. **1988**, 64, 3153.
- [25] Artman, J. O.; Murphy, J. C.; Foner, S. Phys. Rev. **1965**, 138, A912.
- [26] Williamson, G. K.; Hall, W. H. Acta Metallurgica **1953**, 1, 22.

[27] Smith, C. S.; Stickley, E. E. Phys. Rev. **1943**, 64, 191.